University of Zurich[UZH]

Zurich Open Repository and Archive
University of Zurich
University Library
Strickhofstrasse 39
CH-8057 Zurich
www.zora.uzh.ch

Year: 2020

A Feynman diagram description of the 2D-Raman-THz response of amorphous ice

Sidler, David ; Hamm, Peter

Abstract: The 2D-Raman-THz response in all possible time-orderings (Raman-THz-THz, THz-Raman-THz, and THz-THz-Raman) of amorphous water ice is calculated in two ways: from atomistic molecular dynamics simulations and with the help of a Feynman diagram model, the latter of which power-expands the potential energy surface and the dipole and polarizability surfaces up to leading order. Comparing both results allows one to dissect the 2D-Raman-THz response into contributions from mechanical anharmonicity, as well as electrical dipole and polarizability anharmonicities. Mechanical anharmonicity dominates the 2D-Raman-THz response of the hydrogen-bond stretching and hydrogen-bond bending bands of water, and dipole anharmonicity dominates that of the librational band, while the contribution of polarizability anharmonicity is comparably weak. A distinct echo of the hydrogen-bond stretching band is observed for the THz-Raman-THz pulse sequence, again dominated by mechanical anharmonicity. A peculiar mechanism is discussed, which is based on the coupling between the many normal modes within the hydrogen-bond stretching band and which will inevitably generate such an echo for an amorphous structure.

DOI: https://doi.org/10.1063/5.0018485

Posted at the Zurich Open Repository and Archive, University of Zurich
ZORA URL: https://doi.org/10.5167/uzh-198689
Journal Article
Accepted Version

Originally published at:
Sidler, David; Hamm, Peter (2020). A Feynman diagram description of the 2D-Raman-THz response of amorphous ice. Journal of Chemical Physics, 153(4):044502.
DOI: https://doi.org/10.1063/5.0018485

A Feynman Diagram Description of the 2D-Raman-THz Response of Amorphous Ice

David Sidler, Peter Hamm
Department of Chemistry, University of Zurich,
Winterthurerstr. 190, CH-8057 Zürich, Switzerland
peter.hamm@chem.uzh.ch
(Dated: July 9, 2020)

The 2D-Raman-THz response in all possible time-orderings (Raman-THz-THz, THz-Raman-THz and THz-THz-Raman) of amorphous water ice is calculated in two ways: from atomistic molecular dynamics simulations, and with the help of a Feynman diagram model, the latter of which power-expands the potential energy surface and the dipole and polarizability surfaces up to leading order. Comparing both results allows one to dissect the 2D-Raman-THz response into contributions from mechanical anharmonicity, as well as electrical dipole and polarizability anharmonicities. Mechanical anharmonicity dominates the 2D-Raman-THz response of the hydrogen-bond stretching and hydrogen-bond bending bands of water and dipole anharmonicity that of the librational band, while the contribution of polarizability anharmonicity is comparably weak. A distinct echo of the hydrogen-bond stretching band is observed for THz-Raman-THz pulse sequence, again dominated by mechanical anharmonicity. A peculiar mechanism is discussed, which is based on the coupling between the many normal modes within the hydrogen-bond stretching band, and which will inevitably generate such an echo for an amorphous structure.

I. INTRODUCTION

Water is the most abundant liquid, but one with very peculiar thermodynamical properties.[1] The intermolecular forces determine those properties, and at the same time also the low-frequency, intermolecular vibrational spectra. The latter may provide information on the intermolecular forces, however, the conventional, i.e., one-dimensional (1D), THz and Raman spectra of liquid water are very blurred and the information content that can be extracted from them is quite limited. Extending the spectra into two dimensions by 2D spectroscopy may increase the resolution of those convoluted spectra. With this in mind, Tanimura and Mukamel proposed 2D-Raman spectroscopy in a seminal paper,[2] which has been succeeded by numerous theoretical[3–19] and experimental works.[20–27] The low-frequency counterpart of 2D-IR spectroscopy,[28,29] 2D-THz spectroscopy, has been demonstrated as well,[30–37] but neither 2D-Raman nor 2D-THz spectroscopy became possible for water as of now.[38]

To circumvent the prevailing cascaded 3rd-order signal in 2D-Raman spectroscopy,[10,21,24,39] we proposed more recently a hybrid method, 2D-Raman-THz spectroscopy.[40–42] 2D-Raman-THz hybrid spectroscopy is conceptually very similar to 2D-Raman spectroscopy. That is, the system under study is perturbed twice by two Raman interactions in 2D-Raman spectroscopy, and is then read out via a 3rd Raman interaction (RRR pulse sequence). Hybrid 2D-Raman-THz spectroscopy replaces two of the Raman interactions with THz interactions, resulting in three possible time orderings, RTT, TRT, and TTR, all of which have been realized by now experimentally on water,[43,44] aqueous salt solutions,[45] as well as bromoform and related liquids.[46–48] The theory of 2D-Raman-THz spectroscopy is continuously been developed.[40–42,49–60]

The basic goal of 2D-Raman-THz (and 2D-Raman) spectroscopy is the same as that of "conventional" 2D-IR[28,29] (and 2D-THz) spectroscopy, i.e., determining spectroscopic inhomogeneities and couplings between different spectroscopic degrees of freedom. However, the number of light-matter interactions is different in both classes of 2D spectroscopy. That is, 2D-Raman-THz spectroscopy works with in total three interactions ("2-in-1-out"), while 2D-IR spectroscopy uses four of them ("3-in-1-out").[61] Based on the number of interactions in 2D-Raman-THz spectroscopy, one can easily count that at least one of them must induce a zero-quantum or a two-quantum transition (which would be forbidden in the harmonic limit), while 2D-IR spectroscopy requires only one-quantum transitions.

As a consequence, the appearance of 2D-Raman-THz spectra is significantly more complex, as illustrated in Fig. 1 for two coupled modes. Both 2D-Raman-THz and 2D-IR spectroscopy consist of in total 16 coherence pathways, but they are distributed much more regularly in a 2D-IR spectrum (Fig. 1, left). That is, a 2D-IR spectroscopy consist of effectively only 4 peaks in the non-rephasing quadrant (with $\omega_1 > 0$ and $\omega_2 > 0$), two diagonal peaks ($\tilde{A}$ and $\tilde{B}$) and a set of two symmetric cross peaks ($\tilde{C}$ and $\tilde{D}$), each of which complemented by an anharmonically shifted counterpart with opposite sign (shown as open circles in Fig. 1, left). In addition, a symmetric set of peaks exists in the rephasing quadrant (with $\omega_1 < 0$ and $\omega_2 > 0$, i.e., $\tilde{A}'$, $\tilde{B}'$, $\tilde{C}'$ and $\tilde{D}'$); in fact, most applications of 2D-IR spectroscopy add up rephasing (after inverting ω_1) and non-rephasing spectra to reveal a "purely absorptive" spectrum.[62]

None of these symmetries exists for 2D-Raman-THz spectroscopy. Using established rules for Feynman diagrams,[29] one can collect all possible coherence pathways shown in Fig. 1 (right). We consider only the lowest-order coherence pathways with only one zero-quantum

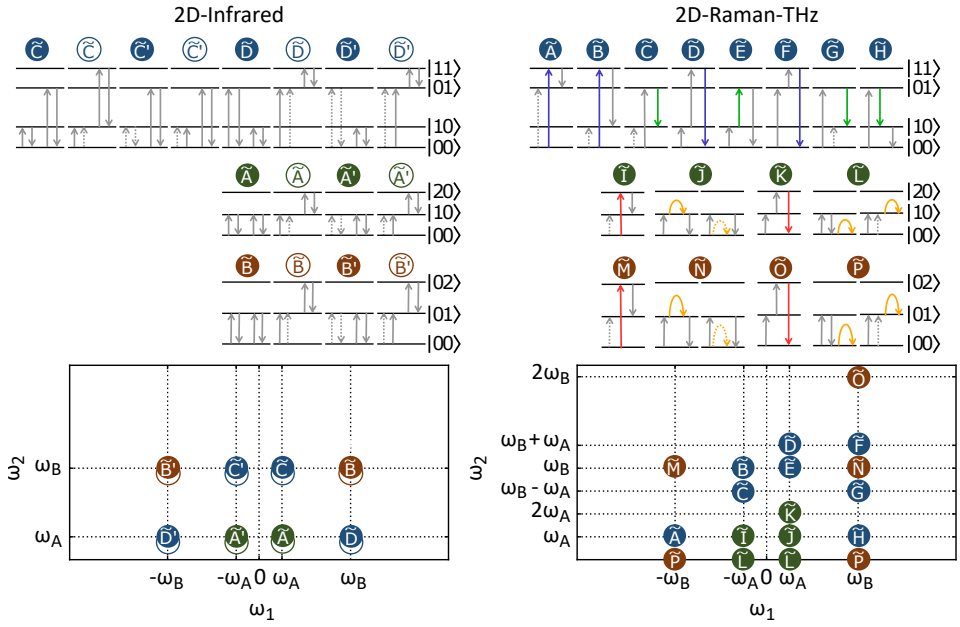

FIG. 1. Schematic 2D spectra for "conventional" 2D-IR (or 2D-THz) spectroscopy (left) as well as for 2D-Raman-THz (or 2D-Raman) spectroscopy (right). For each peak, the coherence diagram is drawn above the spectrum, in which solid arrows indicate transitions caused by action on the ket side of the density matrix, and dotted arrows on the bra side. Grey arrows indicate one-quantum transitions and yellow arrows zero-quantum transitions. Two-quantum transitions are subdivided in double-(de)excitations (red), simultaneous (de)excitations of both modes (blue) and excitation transfer (green). Blue circles are cross peaks between oscillators A and B, green circles are diagonal peaks of A, and brown circles mark diagonal peaks of oscillator B.

(yellow arrows in Fig. 1), or one two-quantum transition, for either the first, second or third field interaction, facilitated by electrical or mechanical (cross)-anharmonicity, the details of which will be derived in Sec. III. A two-quantum transition can either be a double-(de)excitation of a single mode ($|00\rangle \leftrightarrow |20\rangle$ or $|00\rangle \leftrightarrow |02\rangle$, red arrows in Fig. 1), simultaneous (de)excitation of both modes ($|00\rangle \leftrightarrow |11\rangle$, blue arrows), or excitation transfer ($|01\rangle \leftrightarrow |10\rangle$, green arrows).

The essential aim of this paper is to learn how to disentangle complicated 2D-Raman-THz spectra and to extract the dominant coupling mechanisms from observed cross peaks. The molecular system we selected for this purpose is amorphous water ice. While no experimental data exist on amorphous ice as of now, we have studied liquid water extensively.[43–45] The structural motifs in amorphous ice are very similar to its liquid counterpart, but the dynamics is in the inhomogeneous limit with diffusive motion completely suppressed. Amorphous ice results in higher resolved spectra, which will be a prerequisite for being able to disentangle the many diagonal and cross-peak contributions to the 2D-Raman-THz spectra.

We start in Sec. II with calculating 2D-Raman-THz spectra of amorphous ice from atomistic molecular dynamics (MD) simulations, and then develop in Sec. III the theory of 2D-Raman-THz spectroscopy of coupled modes along the lines of Fig. 1. The theory we present is similar in flavor as what has been done in the context of 2D-Raman spectroscopy[4,6,7,12] or infrared-infrared-visible spectroscopy,[51] but with a focus on further understanding the effect of mechanical anharmonicity. By describing the effect of anharmonic couplings on transition probabilities in the simplest possible terms, we gain direct insight into the signal generation mechanism. With that, we deconvolute the 2D-Raman-THz spectra obtained from MD into simpler "anharmonicity spectra" (as we will call them), which facilitate the discussion of certain spectroscopic features, such as the observed echo.

II. 2D-RAMAN-THZ SPECTRA FROM MOLECULAR DYNAMICS SIMULATIONS

A. Methods

The quantum mechanical response functions to calculate the three different time-orderings of 2D-Raman-THz spectroscopy are:[40,50]

$$\begin{aligned} R^{(MD)}_{RTT}(t_1,t_2) &\propto -\mathrm{Tr}\big(\hat{\mu}(t_1+t_2)\,[\hat{\mu}(t_1),[\hat{\alpha}(0),\rho_{\mathrm{eq}}]]\,\big) \\ R^{(MD)}_{TRT}(t_1,t_2) &\propto -\mathrm{Tr}\big(\hat{\mu}(t_1+t_2)\,[\hat{\alpha}(t_1),[\hat{\mu}(0),\rho_{\mathrm{eq}}]]\,\big) \\ R^{(MD)}_{TTR}(t_1,t_2) &\propto -\mathrm{Tr}\big(\hat{\alpha}(t_1+t_2)\,[\hat{\mu}(t_1),[\hat{\mu}(0),\rho_{\mathrm{eq}}]]\,\big) \end{aligned} \quad (1)$$

Depending on the positions of THz and Raman interactions in the pulse sequence, either the dipole ($\hat{\mu}(t)$) or the polarizability ($\hat{\alpha}(t)$) operator appears at the corresponding times in these correlation functions. In order

to derive them from atomistic MD simulations, we used a hybrid equilibrium-nonequilibrium approach, which has initially been developed by Y. Tanimura and coworkers in the context of 2D-Raman spectroscopy,[18], but which can easily be adapted for 2D-Raman-THz spectroscopy.[42]

We chose TL4P^{a2}-CT as a rigid, intrinsically polarizable water force field for the MD simulations.[63] TL4P^{a2}-CT is an extension of TL4P,[64] which has been shown to reveal a reasonable agreement with experimental 2D-Raman-THz spectra of liquid water,[42] but has been amended with two features for a more realistic description of the intensities of all spectroscopic features in the 1D THz and Raman spectra: charge transfer (CT) between hydrogen-bonded water molecules, and a slightly anisotropic polarizability. Details can be found in Ref. 63.

A cubic box containing 64 such water molecules subject to periodic boundary conditions defines our system. Liquid water was simulated at 300 K (thermostated with a time-constant of 1 ps) at experimental density in the NVT ensemble, with time-step 2.5 fs. To generate amorphous ice, the simulation box was first expanded to a density of 0.94 g/cm^3, which is the typical density of low density amorphous ice.[65] Because the amorphous ice structures remain stable for essentially infinite time, sampling of the complete phase space requires a set of different starting structures. A collection of 2000 reference structures were generated by randomizing initial velocities of the starting structure, followed by 40 ps of randomization at 500 K. The structures were then equilibrated at 300 K for 40 ps, and finally cooled down to 70 K during 400 ps, using a coupling constant of 20 ps for the thermostat, which served as starting points for the calculation of Eq. 1. Since diffusive motion is absent, the 2D-Raman-THz responses of in amorphous ice converge about 10 times faster than for the liquid; total simulation times of 120 μs and 12 μs went into the calculation of Fig. 3a,b and Fig. 3c,d, respectively.

B. Spectra

Fig. 2 shows 1D THz (a) and Raman (b) spectra of liquid water at room temperature (red) and amorphous ice at 70 K (blue), calculated from the dipole-dipole and polarizability-polarizability correlation functions, respectively:

$$I_{\mathrm{THz}}(\omega) = \Im \int_0^\infty \langle \mu(t)\dot{\mu}(0) e^{i\omega t} dt \qquad (2)$$

$$I_{\mathrm{Raman}}(\omega) = \Im \int_0^\infty \langle \alpha(t)\dot{\alpha}(0) e^{i\omega t} dt.$$

The spectra of amorphous ice sharpen up in comparison to those of the liquid, and peaks shift to higher frequencies; the latter reflects the anharmonicity of the intermolecular modes. The contribution around frequency zero, assigned to diffusive motion in the liquid, are freezing out in amorphous ice. In each spectrum, three bands

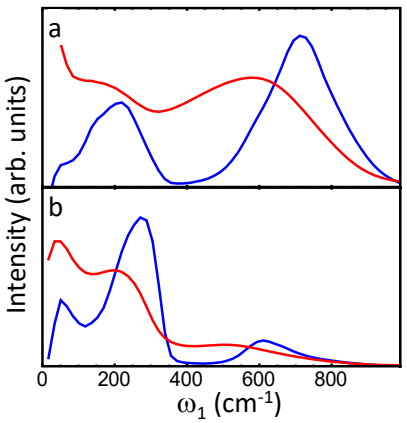

FIG. 2. Simulated (a) THz and (b) $xxxx$-component of Raman spectra of liquid water at room temperature (red) and amorphous ice at 70 K (blue), calculated from the dipole-dipole and polarizability-polarizability correlation functions, respectively, see Eq. 2

can be detected, albeit with different intensities and peak frequencies. The highest frequency peak at about 700 cm^{-1} in the THz spectrum of amorphous ice, or 600 cm^{-1} in the Raman spectrum, is the librational band, i.e., a hindered rotation. The band at 210 cm^{-1} (THz) or 270 cm^{-1} (Raman) is the hydrogen-bond vibration, and the peak at around 60 cm^{-1} in the Raman spectrum (which shows up only as shoulder in the THz spectrum) the hydrogen-bond-bending. The different intensities of these bands reflect the different transition probabilities, e.g., the librational band is strong in the THz spectrum, since a rotating dipole couples strongly to the electromagnetic field, while a rotating, almost isotropic polarizability does not. In turn, the slightly different peak frequencies are known as the non-coincidence effect,[66] and reflect the delocalisation of these modes over a certain number of water molecules, in which case the different selection rules of Raman and THz spectroscopy set in.

Fig. 3a,c show simulated 2D-Raman-THz responses in the time domain of liquid water and amorphous ice, respectively, for the three possible time-orderings RTT, TRT, and TTR. The coherence lifetimes for amorphous ice (Fig. 3c) are significantly longer than in liquid water (Fig. 3a), and the signal expands well past 0.5 ps. The stretched contributions along the t_1 or t_2 axes, which dominate the response in the liquid also, are largely suppressed in the solid. Instead, an echo signal becomes evident in the TRT pulse sequence (marked by an arrow in Fig. 3c).

In accordance with the longer coherence lifetime observed in the time-domain, the frequency domain spectra, taking the real-part of the Fourier transformation, are significantly more structured in the case of amorphous ice as compared to liquid water (Fig. 3b,d). We obtain a very rich 2D-Raman-THz spectra, containing diagonal as well as cross-peaks between the various spectroscopic features introduced in the context of Fig. 2.

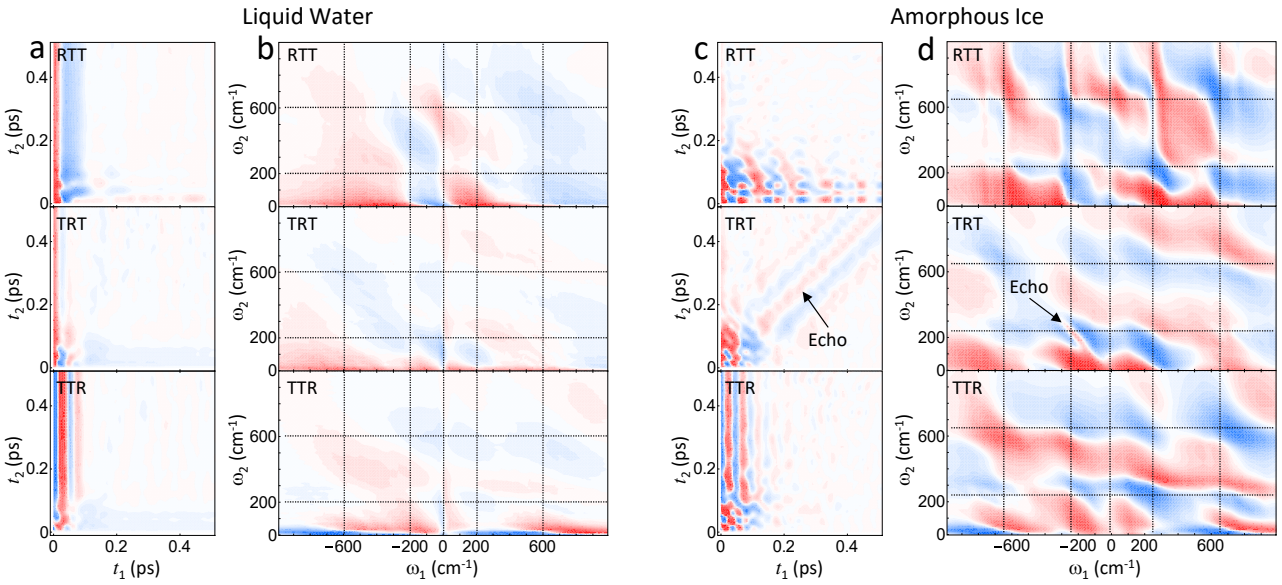

FIG. 3. 2D-Raman-THz spectra with the RTT, TRT and TTR time-orderings ($xxxx$-components) for liquid water (panels a,b) and amorphous ice (panels c,d) obtained from MD simulations. The responses are shown in the time domain (panels a,c) as well as in the frequency domain (panels b,d). The grid lines mark the positions of the dominating hydrogen-bond stretching and librational modes. For amorphous ice, an echo feature is visible in the TRT pulse sequence, which is discussed in the text.

Each spectrum is of equal complexity as Fig. 1, but the three time-orderings weight the various 2D features differently, reflecting the different transition probabilities of THz and Raman interactions. The aim of the paper is to assign these complicated 2D-Raman-THz spectra (we will consider the amorphous ice spectra only from now on).

One feature deserves a special discussion here: In the time-domain data of the TRT pulse sequence, we find a very long-lived echo, which in the frequency-domain results in a very sharp diagonal feature in the rephasing quadrant with $\omega_1 < 0$ and $\omega_2 > 0$ (marked by an arrow in Fig. 3d). That feature is broad in the diagonal direction but very narrow in the anti-diagonal direction. From its frequency, we conclude that the echo is related to the hydrogen-bond stretch vibration around 200 cm^{-1}. Interestingly, the sharp echo-feature sits atop of a much broader feature, also on the diagonal but with opposite sign. These two types of diagonal peaks will become an important point. That is, what we call a "band" in the 1D THz or Raman spectra is actually a collection of very many normal modes; as many as there are water molecules. Cross peaks between those normal modes do appear around the diagonal of the 2D-Raman-THz spectrum, and they are responsible for the broad feature. On the other hand, for an echo to build up, the transition frequency during time periods t_1 and t_2 needs to be correlated. That is possible only is the system is in a $|0\rangle\langle 1|$-coherence of a mode during period t_1, and in a $|2\rangle\langle 1|$-coherence of one and the same mode during period t_2. If the mode is close to harmonic, the $|0\rangle\langle 1|$-frequency is about the same as the $|2\rangle\langle 1|$-frequency, albeit with opposite sign, and strongly correlated, which is a prerequisite for the "inversion of coherence" needed to generate an echo.[61] We will see in Sec. IV that there are two distinctively different possibilities to generate this situations.

III. 2D-RAMAN THZ-SPECTRA FROM A FEYNMAN-DIAGRAM PICTURE

The following theory extends previous works[4,6,7,12,51] by also including the effect of mechanical anharmonicity, which we will see plays a dominant role in the signal generation.

A. Hamiltonian

The motion of a harmonic system can be described as the sum of independent normal mode coordinates $\hat{q}_A$ with the Hamiltonian

$$\hat{H}_A^{(0)} = \tfrac{1}{2}\hbar\omega_A\left(\hat{p}_A^2 + \hat{q}_A^2\right). \tag{3}$$

Furthermore, in order to describe light-matter interactions, dipole and polarizability operators are needed, which are usually expanded in powers of position operators. In the harmonic limit, the linear terms

$$\begin{aligned}\hat{\mu}_A^{(0)} &= \mu_A\hat{q}_A \\ \hat{\alpha}_A^{(0)} &= \alpha_A\hat{q}_A\end{aligned} \tag{4}$$

are sufficient. We will consider pairwise two normal modes, A and B, with $\hat{q}_A$ and $\hat{q}_B$, respectively, which

decouple in the harmonic limit. The solution for the 2D oscillator is given by product states:

$$|m,n\rangle \equiv \varphi_m(q_A)\varphi_n(q_B), \tag{5}$$

where m is the quantum number describing the state of oscillator A, and n is the quantum number of oscillator B.

However, a perfectly harmonic system does not generate any 2D-Raman-THz signal, as it allows only single-quantum transitions.[61] The lowest order deviations from the harmonic case are treated either as corrections to dipole and polarizability operators (electrical anharmonicity):

$$\begin{aligned}\hat{\mu}^{(1)}_{AB} &= \mu_{AB}\hat{q}_A\hat{q}_B \\ \hat{\alpha}^{(1)}_{AB} &= \alpha_{AB}\hat{q}_A\hat{q}_B\end{aligned} \tag{6}$$

or as perturbations to the Hamiltonian (mechanical anharmonicity):

$$\hat{H}^{(1)}_{AB} = \hbar\omega_A\lambda_{AAB}\hat{q}^2_A\hat{q}_B \tag{7}$$

These expressions include "one-body" terms with $A = B$ as well as "two-body" terms with $A \neq B$. Since we will eventually sum over all modes A and B, Eq. 7 also includes the complementary term λ_{ABB}.

B. Ladder Operators

In order to determine the light-matter interaction by time-dependent perturbation theory, we need to know the transitions induced by the dipole $\hat{\mu}$ and polarizability $\hat{\alpha}$ operators. As these operators are expanded in position operators, it is sufficient to know the transitions caused by the operators $\hat{q}_A$ and $\hat{q}_B$. Expressing these operators in terms of ladder operators gives a very simple interpretation for the action of a position operator on the wave function:

$$\begin{aligned}\hat{q}_A &= \tfrac{1}{\sqrt{2}}\left(\hat{a}_A + \hat{a}^\dagger_A\right) \\ \hat{q}_B &= \tfrac{1}{\sqrt{2}}\left(\hat{a}_B + \hat{a}^\dagger_B\right).\end{aligned} \tag{8}$$

Action of a ladder operator excites or de-excites the state by one quantum. Operators $\hat{q}_A$ and $\hat{q}_B$ therefore cause transitions $|00\rangle \leftrightarrow |10\rangle$ and $|00\rangle \leftrightarrow |01\rangle$, respectively, revealing the selection rules of the harmonic oscillator.

1. *Electrical Anharmonicity*

The effect of electrical anharmonicity can be derived in the same way. That is, expressing the product $\hat{q}_A\hat{q}_B$ (Eq. 6) in the form of ladder operators gives:

$$\begin{aligned}\hat{q}_A\hat{q}_B &= \tfrac{1}{2}\left(\hat{a}^\dagger_A + \hat{a}_A\right)\left(\hat{a}^\dagger_B + \hat{a}_B\right) \\ &= \tfrac{1}{2}(\hat{a}^\dagger_A\hat{a}^\dagger_B + \hat{a}_A\hat{a}_B) + \tfrac{1}{2}(\hat{a}^\dagger_A\hat{a}_B + \hat{a}_A\hat{a}^\dagger_B),\end{aligned} \tag{9}$$

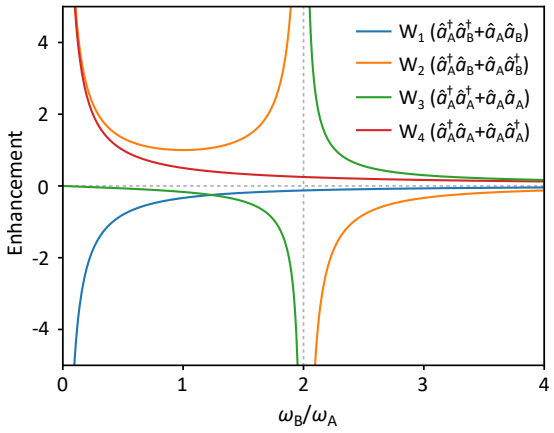

FIG. 4. Frequency dependent factors W_1 - W_4, that scale the response functions caused by anharmonic coupling λ_{AAB}.

where the two terms $\hat{a}^\dagger_A\hat{a}^\dagger_B$ and $\hat{a}_A\hat{a}_B$ cause $|00\rangle \leftrightarrow |11\rangle$ transitions (simultaneous excitation or de-excitation), whereas $\hat{a}^\dagger_A\hat{a}_B$ and $\hat{a}_A\hat{a}^\dagger_B$ cause $|01\rangle \leftrightarrow |10\rangle$ transitions (excitation transfer). For the one-body terms with $A = B$, the two terms $\hat{a}^{\dagger 2}_A$ and $\hat{a}^2_A$ cause double-excitations $|00\rangle \leftrightarrow |20\rangle$ of mode A, while $\hat{a}^\dagger_A\hat{a}_A$ and $\hat{a}_A\hat{a}^\dagger_A$ cause zero-quantum transitions $|00\rangle \leftrightarrow |00\rangle$.

2. *Mechanical Anharmonicity*

The treatment of mechanical anharmonicity is more involved. That is, although the position operators $\hat{q}_A$ and $\hat{q}_B$ *per se* are not affected by the anharmonic perturbation Eq. 7, their representations in an anharmonic eigenstate basis are. As derived in Appendix A, operators $\hat{q}_A$ and $\hat{q}_B$ take the form:

$$\begin{aligned}\hat{q}_A = &\underbrace{\tfrac{1}{\sqrt{2}}\left(\hat{a}^\dagger_A + \hat{a}_A\right)}_{\hat{q}^H_A} \\ &+ \lambda_{AAB}\underbrace{\left[W_1\left(\hat{a}_A\hat{a}_B + \hat{a}^\dagger_A\hat{a}^\dagger_B\right) + W_2\left(\hat{a}^\dagger_A\hat{a}_B + \hat{a}_A\hat{a}^\dagger_B\right)\right]}_{\hat{q}^{AAB}_A}\end{aligned} \tag{10}$$

$$\begin{aligned}\hat{q}_B = &\underbrace{\tfrac{1}{\sqrt{2}}\left(\hat{a}^\dagger_B + \hat{a}_B\right)}_{\hat{q}^H_B} \\ &+ \lambda_{AAB}\underbrace{\left[W_3\left(\hat{a}^{\dagger 2}_A + \hat{a}^2_A\right) + W_4\left(\hat{a}^\dagger_A\hat{a}_A + \hat{a}_A\hat{a}^\dagger_A\right)\right]}_{\hat{q}^{AAB}_B}\end{aligned} \tag{11}$$

with:

$$W_1 = \frac{1}{2}\left(\frac{1}{2+\omega} - \frac{1}{\omega}\right)$$
$$W_2 = \frac{1}{2}\left(\frac{1}{2-\omega} + \frac{1}{\omega}\right)$$
$$W_3 = \frac{1}{4}\left(\frac{1}{2+\omega} - \frac{1}{2-\omega}\right)$$
$$W_4 = \frac{1}{2}\left(\frac{1}{\omega}\right) \tag{12}$$

and $\omega = \omega_B/\omega_A$. W_2 and W_3 diverge for $\omega_B = 2\omega_A$ (Fermi resonance), and W_1, W_2 and W_4 for $\omega_B \ll \omega_A$, see Fig. 4.

The first terms in Eqs. 10 and 11 are simply $\hat{q}_A$ and $\hat{q}_B$ in harmonic eigenstate basis (we will call them $\hat{q}_A^H$ and $\hat{q}_B^H$ from now on). With regard to the anharmonic perturbation, however, the action of $\hat{q}_A$ and $\hat{q}_B$ is distinctively different. That is, $\hat{q}_A$ reveals terms containing $\hat{a}_A\hat{a}_B$ and $\hat{a}_A^\dagger\hat{a}_B^\dagger$, which allow for the simultaneous excitation or de-excitation of both oscillators $|00\rangle \leftrightarrow |11\rangle$, and terms containing $\hat{a}_A^\dagger\hat{a}_B$ and $\hat{a}_A\hat{a}_B^\dagger$, which cause excitation transfer $|10\rangle \leftrightarrow |01\rangle$.

Operator $\hat{q}_B$, in turn, contains terms $\hat{a}_A^{\dagger 2}$ and $\hat{a}_A^2$, inducing double excitations of oscillator A, $|00\rangle \leftrightarrow |20\rangle$, as well as terms $\hat{a}_A^\dagger\hat{a}_A$ and $\hat{a}_A\hat{a}_A^\dagger$ inducing zero-quantum transitions $|10\rangle \leftrightarrow |10\rangle$ (shown in yellow in Fig. 1). Despite the fact that these are two-body terms originate from a coupling between mode A and B via λ_{AAB}, they cause contributions to a 2D spectrum at the same frequency positions as electrical one-body terms (see Sec. III B 1).

If nonlinearities μ_{AB}, α_{AB} andλ_{AAB} are each considered to be a small perturbation, we can ignore cross terms including more than one of these perturbations, and express the dipole and polarizability operators as:

$$\begin{aligned}\hat{\mu} =& \mu_A\hat{q}_A^H + \mu_B\hat{q}_B^H + \mu_{AB}\hat{q}_A^H\hat{q}_B^H \\ &+ \lambda_{AAB}\left(\mu_A\hat{q}_A^{AAB} + \mu_B\hat{q}_B^{AAB}\right) \\ \hat{\alpha} =& \alpha_A\hat{q}_A^H + \alpha_B\hat{q}_B^H + \alpha_{AB}\hat{q}_A^H\hat{q}_B^H \\ &+ \lambda_{AAB}\left(\alpha_A\hat{q}_A^{AAB} + \alpha_B\hat{q}_B^{AAB}\right),\end{aligned} \tag{13}$$

where the definitions of the various position operators are given in Eqs. 10 and 11. We furthermore assume that mechanical anharmonicity predominantly affects the transition dipoles and transition polarizabilities, while we ignore the change in energy levels. In that limit, it is sufficient to consider only pathways starting from the ground state $\rho_{\mathrm{eq}} = |00\rangle\langle 00|$, and the response remains temperature independent.[59]

C. Basis Responses

Having expressions for dipole and polarizability operators (Eq. 13), the 2D-Raman-THz responses can be derived based on time-dependent perturbation theory (Eq. 1). We will illustrate the procedure for one of the simpler examples, R^α_{TRT}, i.e., the 2D-Raman THz response in the TRT pulse sequence, which breaks the harmonic selection rules via the nonlinear polarizability α_{AB}. The contribution of R^α_{TRT} to the total response Eq. 1 is:

$$R^\alpha_{\mathrm{TRT}}(t_1,t_2) = -\mathrm{Tr}\big(\hat{q}_B^H(t_1+t_2)[\hat{q}_A^H\hat{q}_B^H(t_1),[\hat{q}_A^H(0),\rho_{eq}]]\big) \tag{14}$$

which scales with a product of transition probabilities and the nonlinear polarizability $\mu_B\alpha_{AB}\mu_A$. It gives rise to 2 peaks in the 2D spectrum, i. e., peaks $\tilde{E}$ and $\tilde{B}$ in Fig. 1 (right). Peak $\tilde{E}$ starts with single quantum transition of oscillator A, reaching $|10\rangle\langle 00|$ on the ket-side of the density matrix at time 0, which oscillates with frequency $+\omega_A$ during time-period t_1. The nonlinear second interaction then causes an excitation transfer via $\hat{a}_A\hat{a}_B^\dagger$ of Eq. 9, reaching $|01\rangle\langle 00|$ that oscillates at frequency $+\omega_B$ during time-period t_2. The last interaction at time t_1+t_2 brings the system back to $|00\rangle\langle 00|$ via a single-quantum de-excitation of mode B. For peak $\tilde{B}$, the first interaction works on the bra-side, reaching $|00\rangle\langle 10|$ that oscillates at frequency $-\omega_A$. Now, the $\hat{a}_A^\dagger\hat{a}_B^\dagger$-term of Eq. 9 sets in for the second, nonlinear interaction on the ket-side, revealing $|11\rangle\langle 10|$ oscillating at frequency $+\omega_B$. The last interaction goes down to $|10\rangle\langle 10|$. Peaks $\tilde{E}$ and $\tilde{B}$ are equally strong, but have opposite signs, which can be seen when expanding the commutators in Eq. 14. The corresponding response function is in the time domain:

$$\begin{aligned}R^\alpha_{\mathrm{TRT}}(t_1,t_2) = e^{-\frac{\gamma_A}{2}t_1-\frac{\gamma_B}{2}t_2}\big(&\cos(-\omega_A t_1+\omega_B t_2) \\ &-\cos(+\omega_A t_1+\omega_B t_2)\big),\end{aligned} \tag{15}$$

where we introduced in addition relaxation terms derived from a Brownian oscillator model.[12]

Considering all sources of nonlinearity, we have to consider five such response functions:

$$\begin{aligned}R_o^{tot}(t_1,t_2) = \sum_{A,B}\big(&\lambda_{AAB}\mu_A^2\alpha_B R_o^{\lambda_1}(t_1,t_2) \\ &+\lambda_{AAB}\mu_A\mu_B\alpha_A R_o^{\lambda_2}(t_1,t_2) \\ &+\mu_{AB}\mu_A\alpha_B R_o^{\mu_1}(t_1,t_2) \\ &+\mu_{AB}\mu_B\alpha_A R_o^{\mu_2}(t_1,t_2) \\ &+\alpha_{AB}\mu_A\mu_B R_o^{\alpha}(t_1,t_2)\big),\end{aligned} \tag{16}$$

where the subscript $o \in \{\mathrm{RTT},\mathrm{TRT},\mathrm{TTR}\}$ indicates one of the time-orderings and we summed over all pairs of modes A and B. To understand that, we need to note that there is only one response function R_o^α, since we have only one Raman interaction in the pulse sequence, hence the nonlinear polarizability α_{AB} can only act at that one time-position. In contrast, mechanical anharmonicity λ_{AAB} and the nonlinear dipole operator μ_{AB} can act on more than one time-position. When grouping them according to their pre-factors ($\lambda_{AAB}\mu_A^2\alpha_B$, $\lambda_{AAB}\mu_A\mu_B\alpha_A$,

TABLE I. Relative peak intensities of the four basis responses R^{λ_1}, R^{λ_2}, R^{μ} and R^{α} for the three pulse sequences RTT, TRT, and TTR of 2D-Raman-THz spectroscopy. The frequency dependent scaling factors W_1 to W_4 are given in Eq. 12. The relaxation terms γ_1 and γ_2 are derived from a Brownian oscillator model.[12]

					RTT				TRT				TTR			
Peak	ω_1	ω_2	γ_1	γ_2	$R^{\lambda_1}_{RTT}$	$R^{\lambda_2}_{RTT}$	R^{μ}_{RTT}	R^{α}_{RTT}	$R^{\lambda_1}_{TRT}$	$R^{\lambda_2}_{TRT}$	R^{μ}_{TRT}	R^{α}_{TRT}	$R^{\lambda_1}_{TTR}$	$R^{\lambda_2}_{TTR}$	R^{μ}_{TTR}	R^{α}_{TTR}
$\tilde{A}$	$-\omega_B$	ω_A	$-\frac{\gamma_B}{2}$	$-\frac{\gamma_A}{2}$	$+W_1$	0	+1	0	0	$+W_1$	0	0	0	$+W_1$	0	0
$\tilde{B}$	$-\omega_A$	ω_B	$-\frac{\gamma_A}{2}$	$-\frac{\gamma_B}{2}$	0	$+W_1$	0	0	0	$+W_1$	0	+1	$+W_1$	0	+1	0
$\tilde{C}$	$-\omega_A$	$\omega_B-\omega_A$	$-\frac{\gamma_A}{2}$	$-\frac{\gamma_A+\gamma_B}{2}$	0	$+W_2$	0	0	$+W_2$	0	+1	0	0	$+W_2$	0	+1
$\tilde{D}$	ω_A	$\omega_A+\omega_B$	$-\frac{\gamma_A}{2}$	$-\frac{\gamma_A+\gamma_B}{2}$	0	$-W_1$	0	0	$-W_1$	0	-1	0	0	$-W_1$	0	-1
$\tilde{E}$	ω_A	ω_B	$-\frac{\gamma_A}{2}$	$-\frac{\gamma_B}{2}$	0	$-W_2$	0	0	0	$-W_2$	0	-1	$-W_2$	0	-1	0
$\tilde{F}$	ω_B	$\omega_A+\omega_B$	$-\frac{\gamma_B}{2}$	$-\frac{\gamma_A+\gamma_B}{2}$	$-W_1$	0	-1	0	0	$-W_1$	0	0	0	$-W_1$	0	0
$\tilde{G}$	ω_B	$\omega_B-\omega_A$	$-\frac{\gamma_B}{2}$	$-\frac{\gamma_A+\gamma_B}{2}$	$+W_2$	0	+1	0	0	$+W_2$	0	0	0	$+W_2$	0	0
$\tilde{H}$	ω_B	ω_A	$-\frac{\gamma_B}{2}$	$-\frac{\gamma_A}{2}$	$-W_2$	0	-1	0	0	$-W_2$	0	0	0	$-W_2$	0	0
$\tilde{I}$	$-\omega_A$	ω_A	$-\frac{\gamma_A}{2}$	$-\frac{\gamma_A}{2}$	0	$+2W_3$	0	0	$+2W_3$	0	0	0	0	$+2W_3$	0	0
$\tilde{J}$	ω_A	ω_A	$-\frac{\gamma_A}{2}$	$-\frac{\gamma_A}{2}$	0	$-2W_4$	0	0	$-2W_4$	0	0	0	0	$-2W_4$	0	0
$\tilde{K}$	ω_A	$2\omega_A$	$-\frac{\gamma_A}{2}$	$-\gamma_A$	0	$-2W_3$	0	0	0	$-2W_3$	0	0	$-2W_3$	0	0	0
$\tilde{L}$	ω_A	0	$-\frac{\gamma_A}{2}$	$-\gamma_A$	0	$+2W_4$	0	0	0	$+2W_4$	0	0	$+2W_4$	0	0	0

$\mu_{AB}\mu_A\alpha_B$ and $\mu_{AB}\mu_B\alpha_A$, respectively), we find two different terms for each one of these possibilities, $R_o^{\lambda_1}$ and $R_o^{\lambda_2}$ as well as $R_o^{\mu_1}$ and $R_o^{\mu_2}$. However, the pre-factors of $R^{\mu 1}$ and $R^{\mu 2}$ are symmetric with respect to A and B, and we can lump them together:

$$\begin{aligned} R_o^{tot}(t_1,t_2) = \sum_{A,B} \big(& \lambda_{AAB}\mu_A^2\alpha_B R_o^{\lambda_1}(t_1,t_2) \\ & +\lambda_{AAB}\mu_A\mu_B\alpha_A R_o^{\lambda_2}(t_1,t_2) \\ & +\mu_{AB}\mu_A\alpha_B R_o^{\mu}(t_1,t_2) \\ & +\alpha_{AB}\mu_A\mu_B R_o^{\alpha}(t_1,t_2)\big). \end{aligned} \tag{17}$$

Deriving these response functions, in the same way as illustrated for $R^{\alpha}_{\mathrm{TRT}}$ (Eq. 15), is tedious but straight forward. They are listed in Table I, and Eq. 15 illustrates how this table is translated into time-domain response functions. Peaks $\tilde{I}$, $\tilde{J}$, $\tilde{K}$ and $\tilde{L}$ look like "diagonal peaks", but really are two-body terms originating from mechanical coupling λ_{AAB} in Eq. 11. To reveal true one-body terms, one has to set $\omega_A = \omega_B$ in Table I, in which case some peaks merge and Table I collapses into Table I of Ref. 59. Peaks $\tilde{M}$, $\tilde{N}$, $\tilde{O}$ and $\tilde{P}$ in Fig. 1 are obtained when interchanging mode A and B, i.e., are related to λ_{ABB}. They are implicitly taken care of in Eq. 17 since the sum runs over all modes A and B.

D. Continuum of States

The number of intermolecular modes present in a condensed phase system such as amorphous ice is enormous, so modes are usually not counted individually, rather they are described by a continuous density of states $D(\omega)$. The variable ω then acts as a collective variable which groups all modes of the same frequency. 2D spectra are scaled by the number of oscillator pairs $D(\omega_A)D(\omega_B)$, and the total response Eq. 17 becomes:

$$\begin{aligned} R_o^{tot}(t_1,t_2) = \int_0^\infty \int_0^\infty d\omega_A d\omega_B \big(& \lambda_1(\omega_A,\omega_B) R_o^{\lambda_1}(t_1,t_2) \\ & +\lambda_2(\omega_A,\omega_B) R_o^{\lambda_2}(t_1,t_2) \\ & +\mu(\omega_A,\omega_B) R_o^{\mu}(t_1,t_2) \\ & +\alpha(\omega_A,\omega_B) R_o^{\alpha}(t_1,t_2)\big) \end{aligned} \tag{18}$$

with

$$\begin{aligned} &\lambda_1(\omega_A,\omega_B) = \\ &\quad D(\omega_A)D(\omega_B)\lambda_{AAB}(\omega_A,\omega_B)\mu_A^2(\omega_A)\alpha_B(\omega_B) \\ &\lambda_2(\omega_A,\omega_B) = \\ &\quad D(\omega_A)D(\omega_B)\lambda_{AAB}(\omega_A,\omega_B)\mu_A(\omega_A)\mu_B(\omega_B)\alpha_A(\omega_A) \\ &\mu(\omega_A,\omega_B) = \\ &\quad D(\omega_A)D(\omega_B)\mu_{AB}(\omega_A,\omega_B)\mu_A(\omega_A)\alpha_B(\omega_B) \\ &\alpha(\omega_A,\omega_B) = \\ &\quad D(\omega_A)D(\omega_B)\alpha_{AB}(\omega_A,\omega_B)\mu_A(\omega_A)\mu_B(\omega_B) \end{aligned} \tag{19}$$

The total response is given as a linear combination of 12 basis responses, $R_o^{\lambda_1}$, $R_o^{\lambda_2}$, R_o^{μ} and R_o^{α} for the three time orderings $o \in \{\mathrm{RTT}, \mathrm{TRT}, \mathrm{TTR}\}$, each of which depends parametrically on ω_A and ω_B (see e.g. Eq. 15). They scale with in total four "anharmonicity spectra" $\lambda_1(\omega_A,\omega_B)$, $\lambda_2(\omega_A,\omega_B)$, $\mu(\omega_A,\omega_B)$ and $\alpha(\omega_A,\omega_B)$, which are universal and are the same for all time-orderings.

E. Anharmonicity Spectra

We calculated those anharmonicity spectra based on quenched normal modes. To that end, snapshot structures were taken from the MD simulation of amorphous

ice, quenched to the next local minimum by gradient decent, and the normal modes $q_{A,B}$ were calculated. The frequencies of these normal modes are given by:

$$\hbar\omega_A = \frac{\partial^2 V}{\partial q_A^2} \tag{20}$$

and the corresponding transition probabilities:

$$\begin{aligned} \mu_A &= \frac{\partial \mu}{\partial q_A} \\ \alpha_A &= \frac{\partial \alpha}{\partial q_A} \end{aligned} \tag{21}$$

The one-body anharmonicity parameters are:

$$\begin{aligned} \mu_{AA} &= \frac{1}{2}\frac{\partial^2 \mu}{\partial q_A^2} \\ \alpha_{AA} &= \frac{1}{2}\frac{\partial^2 \alpha}{\partial q_A^2} \\ \lambda_{AAA} &= \frac{1}{6\hbar\omega_A}\frac{\partial^3 V}{\partial q_A^3} \end{aligned} \tag{22}$$

and the corresponding two-body terms:

$$\begin{aligned} \mu_{AB} &= \frac{\partial^2 \mu}{\partial q_A \partial q_B} \\ \alpha_{AB} &= \frac{\partial^2 \alpha}{\partial q_A \partial q_B} \\ \lambda_{AAB} &= \frac{1}{2\hbar\omega_A}\frac{\partial^2 V}{\partial q_A^2 \partial q_B} \end{aligned} \tag{23}$$

All derivatives were performed numerically. Since we consider the $xxxx$-component of the 2D-Raman-THz spectra in Fig. 3, the x-component of μ and xx-component of α were taken in all derivations. The anharmonicity parameters were multiplied with the corresponding transition probabilities (see Eq. 17), and were binned according to ω_A and ω_B to reveal the anharmonicity spectra $\lambda_1(\omega_A,\omega_B)$, $\lambda_2(\omega_A,\omega_B)$, $\mu(\omega_A,\omega_B)$, and $\alpha(\omega_A,\omega_B)$ shown in Fig. 5, leftmost column. Finally, the 2D-Raman-THz model responses in the three time-orderings RTT, TRT, and TTR were evaluated by Eq. 18, setting $\gamma_A = \gamma_B = (200\text{ fs})^{-1}$. While it is probably an oversimplifying assumption that one universal dephasing time accounts for all degrees of freedom, the value was chosen to properly reproduce the anti-diagonal width of the echo of the hydrogen-bond stretching band (see discussion below). More sophisticated models describing dephasing of intermolecular degrees of freedom have been developed.[15,67]

IV. DISCUSSION

Figs. 5a and 5b compare the MD-simulated 2D-Raman-THz responses with those calculated from the model based on quenched normal modes. Given that the perturbative treatment of the model considers only the leading terms of anharmonicity, the agreement is surprisingly good with the majority of features in the MD-simulated 2D-Raman-THz responses reproduced quite well by the model. Here, it probably helps that we consider amorphous ice instead of liquid water were all degrees of freedom are "locked" and thus explore only the potential energy surface only close to local minima. In liquid water, in contrast, the system would frequently cross barriers between local minima, in which case a low-order power-expansion is likely to fail.

There are indeed features in the MD-simulated 2D-Raman-THz responses, which are missing in the model, and which are encircled in Fig. 5a. The absence of these peaks suggests that some higher-order nonlinear terms are missing in the model. Most of the missing features concerns cross-peaks between the hydrogen-bond stretching band and the librational band (those encircled in green). The frequency ratio of these two bands is roughly 1:3, hence it might be that a terms of the form $q_A^3 q_B$ are missing in the model, which would give rise to a 1:3 Fermi-resonance.

Figs. 5c-f disentangle the model responses into the contributions of the four anharmonicity spectra. We see that mechanical anharmonicity $\lambda_1(\omega_A,\omega_B)$ dominates the overall response, in particular with regard to the lower-frequency hydrogen-bond stretching and bending modes (Figs. 5c). The contribution of mechanical anharmonicity $\lambda_2(\omega_A,\omega_B)$, in contrast, is negligible, presumably due to orientational averaging of its prefactor $\mu_A\mu_B\alpha_A$ (see Eq. 17). When the orientations of mode A and B were uncorrelated, then $\langle\mu_A\mu_B\alpha_A\rangle = \langle\mu_A\alpha_A\rangle\langle\mu_B\rangle = 0$, where $\langle ...\rangle$ is an orientational average. In contrast, the orientational average of $\langle\mu_A^2\rangle\langle\alpha_B\rangle$ for $\lambda_1(\omega_A,\omega_B)$ does not vanish. While the orientations of mode A and B are probably not strictly uncorrelated, since only modes that are coupled by λ_{AAB} contribute, it still appears that the correlation is small enough to strongly suppress the anharmonicity spectrum $\lambda_2(\omega_A,\omega_B)$. This is probably a general conclusion, which is not related to the specific force field and also applies for liquid water.

Electrical dipole anharmonicity $\mu(\omega_A,\omega_B)$ contributes mostly to the librational band, in accordance with the fact that this is also the strongest band in the THz absorption spectrum (Fig. 2a). The contribution of electrical polarizability anharmonicity $\alpha(\omega_A,\omega_B)$ is overall weak, but it is special in the sense that one-body terms along the diagonal stick out.

The last point is connected to the echo observed for the hydrogen-bond stretching band in the TRT pulse sequence. In the time-domain (Fig. 3c), the echo is seen as long-lived signal along the diagonal with $t_1 = t_2$, which translates into a sharp diagonal feature in the rephasing quadrant with $\omega_1 = -\omega_2$ after Fourier transformation into the frequency domain (Figs. 3c and 5a). The echo is well reproduced by the model (Fig. 5b) and the dis-

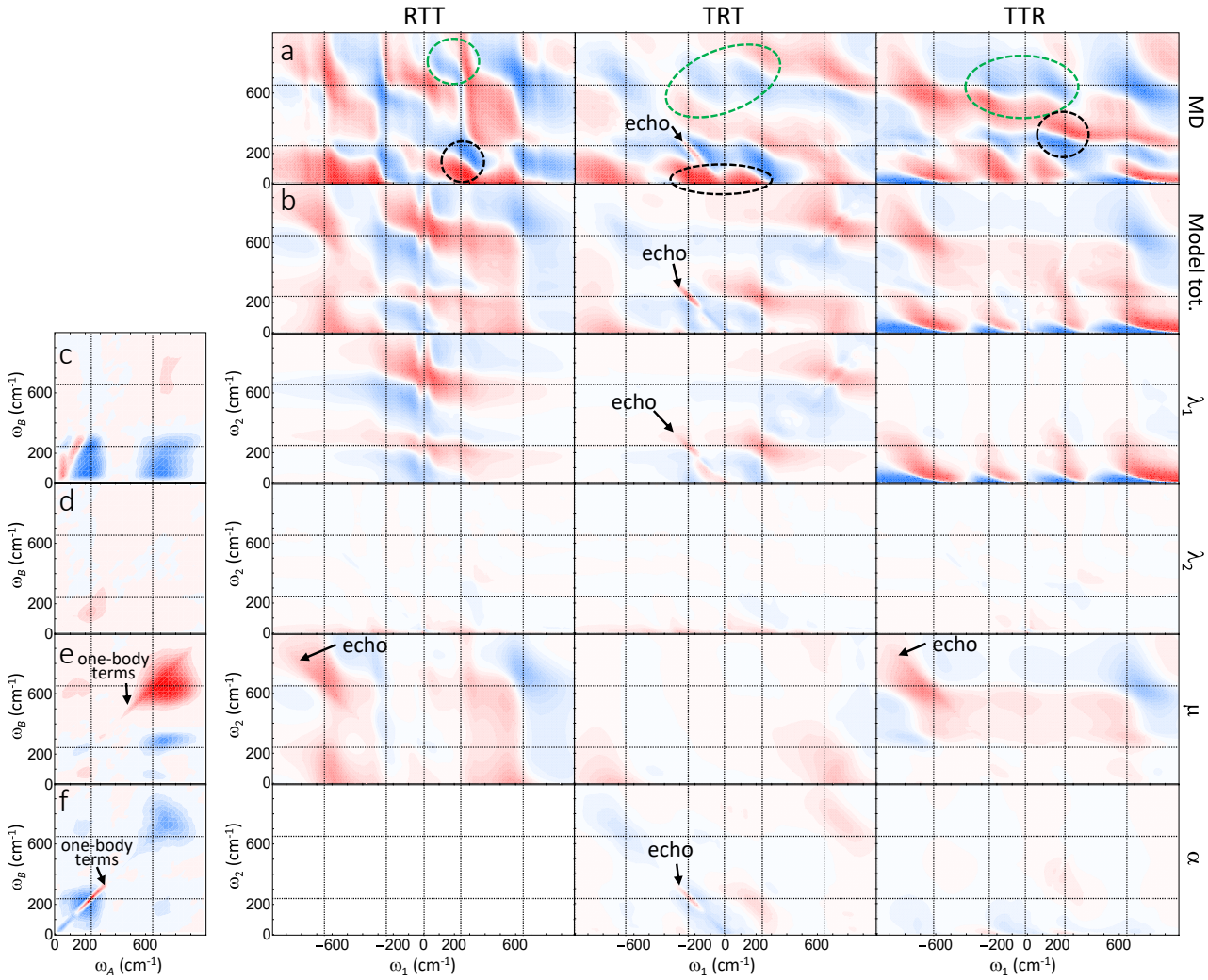

FIG. 5. The 2D-Raman-THz response in the three different time orderings RTT, TRT, and TTR calculated from (a) MD simulations of amorphous ice (same as in Fig. 3d) together with (b) the model response functions calculated from quenched normal modes. Rows (c-f) dissect the model response into the contributions from the various anharmonicity spectra shown in the most left column. The grid lines mark the positions of the dominating hydrogen-bond stretching librational modes. Spectroscopic features that are not reproduced by the model are encircled in row (a). Echo features are labelled.

section of Fig. 5c-f shows that mechanical anharmonicity $\lambda_1(\omega_A, \omega_B)$, and to a somewhat lesser extent polarizability anharmonicity $\alpha(\omega_A, \omega_B)$, contribute to this echo.

An inversion of coherence is needed for an echo to appear. That is, the system needs to be in a $|0\rangle\langle 1|$-coherence of a mode A during time t_1, and in a $|2\rangle\langle 1|$-coherence of one and the same normal mode A during time t_2.[61] For electrical polarizability anharmonicity $\alpha(\omega_A, \omega_B)$, the only diagram that produces this situation is peak $\tilde{B}$ with $\omega_A = \omega_B$ (see Table I), i.e., a one-body term that appears on the diagonal of the anharmonicity spectrum of Fig. 5f (see label).

Mechanical anharmonicity behaves very differently in this regard. Coupling between two different modes A and B by a coupling term λ_{AAB} generates two sets of diagrams, see Eqs. 10 and 11. Despite the fact it needs the couple to another mode B, the second set of diagrams induces transitions in mode A only (Eq. 11), giving rise to peaks $\tilde{I}$ to $\tilde{M}$ (Table I). One of these peaks, $\tilde{I}$, again reveals the inversion of coherence needed for an echo to appear. Peak $\tilde{I}$ exists only in the TRT pulse sequence for $\lambda_1(\omega_A, \omega_B)$. While the anharmonicity spectrum $\lambda_1(\omega_A, \omega_B)$ does have contributions on the diagonal from one-body terms λ_{AAA} (Fig. 5c), the two-body terms dominate in the generation of the echo. This is since the intermolecular low-frequency modes are very delocalized, hence each mode A couples to a large number of modes B via terms λ_{AAB} and their collective contribution is larger than that of the one one-body term λ_{AAA}. In connection with the inhomogeneous broadening of an amorphous structure, mechanical anharmonicity $\lambda_1(\omega_A, \omega_B)$ will inevitably generate a prominent echo in the TRT

pulse sequence.

Experimentally, echoes of the hydrogen-bond stretch vibration have been observed for liquid water[43,44] and aqueous salt solutions[45] only in the RTT pulse sequence. In contrast, the MD simulation reveals an echo for the hydrogen-bond stretch vibration only in the TRT pulse sequence for amorphous ice, and none for liquid water (Fig. 3a). Other MD simulations based on different force fields have revealed hints of an echo also for liquid water, albeit again only in the TRT pulse sequence.[41,53]

Electrical anharmonicity $\mu(\omega_A, \omega_B)$ could potentially generate an echo in the RTT pulse sequence, as observed in experiment, as well as in the TTR pulse sequence. It would have to be one-body terms, for same reason as discussed above for $\alpha(\omega_A, \omega_B)$. In fact one can see a diagonal ridge in $\mu(\omega_A, \omega_B)$ (Fig. 5e, leftmost panel, labelled as "one-body terms"), which indeed gives rise to an echo of the librational band. Also for the librational band, one can see a sharp feature directly on the diagonal of the corresponding 2D-Raman-THz spectra (labelled as echo in (Fig. 5e), accompanied by a much broader feature, however, in contrast to the hydrogen-bond stretch vibration in the TRT pulse sequence, the signs of the two features are not inverted which is why the effect is less distinct.

In a recent paper,[59] we could satisfactorily fit the experimental 2D-Raman-THz spectrum of liquid water with a significantly simpler version of the model introduced here, considering only the hydrogen-bond stretching mode as a single normal mode (the experiment is blind to the librational band, and the hydrogen-bond bending band is weak). In liquid water, the many normal modes within the he hydrogen-bond stretching band interconvert very quickly and the distinction between true one-body terms vs two-body terms that cause couplings between the various normal-modes within that band fades away. This is the reason why one gets away with the much simpler model. Consistent with the discussion above, however, the fit revealed that electrical dipole anharmonicity would have to dominate in order to explain the echo observed for the hydrogen-bond stretching mode in the RTT pulse sequence. This result is not reproduced by MD simulations, for reasons that are currently not understood.

V. CONCLUSION

Amorphous ice is structurally similar to liquid water, but its dynamics is much simpler, resulting in significantly more structured 2D-Raman-THz spectra. Contributions from hydrogen bond bending, hydrogen bond stretching, and librational modes can be distinguished and spectral features can be assigned to specific Feynman pathways. The complicated 2D-Raman-THz spectrum (Fig. 1, right) can thus be deconvoluted into three, much simpler anharmonicity spectra: mechanical anharmonicity $\lambda_1(\omega_A, \omega_B)$, as well as electrical dipole $\mu(\omega_A, \omega_B)$ and polarizability anharmonicity $\alpha(\omega_A, \omega_B)$, which are shown in Fig. 5, leftmost panels (the contribution of $\lambda_2(\omega_A, \omega_B)$ is negligible). The anharmonicity spectra exhibit diagonal and cross-peaks, and can be read in essentially the same was as "conventional" 2D spectra. Electrical dipole anharmonicity $\mu(\omega_A, \omega_B)$ dominates the 2D-Raman-THz response of the librational band, and mechanical anharmonicity $\lambda_1(\omega_A, \omega_B)$ that of the hydrogen bond bending and hydrogen bond stretching band. The latter also dominates the very distinct echo observed in MD simulation in the TRT pulse sequence, while the contribution of electrical polarizability anharmonicity $\alpha(\omega_A, \omega_B)$ is small, in contrast to what has been assumed previously.[41]

The current theory can however not explain the experimentally observed echo in the RTT pulse sequence of liquid water.[43–45] For a better understanding, it would be very important to experimentally measure the 2D-Raman-THz spectrum of amorphous ice, in order to profit from the same resolution gain as we did here with the MD simulations. Work in this direction is currently going on in our lab.

Acknowledgement: The work has been supported by the Swiss National Science Foundation (SNF) through the National Center of Competence and Research (NCCR) MUST as well by the MaxWater network of the Max Planck Society.

Availability of Data: Data available on request from the authors

Appendix A: Position Operators in an Anharmonic Eigenstate Basis

The wave function up to first order in perturbation is given by:

$$|\psi_{k,l}\rangle = |k,l\rangle + \sum_{(i,j)\neq(k,l)} \frac{\langle i,j|\hat{H}^{(1)}|k,l\rangle}{E^0_{i,j} - E^0_{k,l}} |i,j\rangle + \cdots , \quad \text{(A1)}$$

where the perturbed wave function $|\psi_{k,l}\rangle$ is expressed in terms $|k,l\rangle$, the eigenfunctions of the unperturbed system. For a perturbation:

$$\begin{aligned} \hat{H}^{(1)} &= \lambda_{AAB}\hbar\omega_A \hat{q}_A^2 \hat{q}_B \quad \text{(A2)} \\ &= 2^{-3/2}\lambda_{AAB}\hbar\omega_A \\ &\quad \times \left[{a_A^\dagger}^2 + a_A^2 + a_A^\dagger a_A + a_A a_A^\dagger\right]\left[a_B^\dagger + a_B\right]. \end{aligned}$$

the only non-zero matrix elements $|m,n\rangle$ basis are (modulo a factor $2^{-3/2}\lambda_{AAB}\hbar\omega_A$):

$$\begin{aligned}
\left\langle m+2,n+1|\hat{H}^{(1)}|m,n\right\rangle &\propto \sqrt{m+1}\sqrt{m+2}\sqrt{n+1}\\
\left\langle m+2,n-1|\hat{H}^{(1)}|m,n\right\rangle &\propto \sqrt{m+1}\sqrt{m+2}\sqrt{n}\\
\left\langle m,n+1|\hat{H}^{(1)}|m,n\right\rangle &\propto (2m+1)\sqrt{n+1}\\
\left\langle m,n-1|\hat{H}^{(1)}|m,n\right\rangle &\propto (2m+1)\sqrt{n}\\
\left\langle m-2,n+1|\hat{H}^{(1)}|m,n\right\rangle &\propto \sqrt{m}\sqrt{m-1}\sqrt{n+1}\\
\left\langle m-2,n-1|\hat{H}^{(1)}|m,n\right\rangle &\propto \sqrt{m}\sqrt{m-1}\sqrt{n}. \qquad \text{(A3)}
\end{aligned}$$

Therefore, the perturbed wave function according to equation (A1) becomes:

$$\begin{aligned}
|\psi_{m,n}\rangle = |m,n\rangle + 2^{-3/2}\hbar\omega_A\lambda_{AAB} \qquad \text{(A4)}\\
\times\Bigg(\frac{\sqrt{m+1}\sqrt{m+2}\sqrt{n+1}}{\hbar(2\omega_A+\omega_B)} \quad |m+2,n+1\rangle\\
+\frac{\sqrt{m+1}\sqrt{m+2}\sqrt{n}}{\hbar(2\omega_A-\omega_B)} \quad |m+2,n-1\rangle\\
+\frac{(2m+1)\sqrt{n+1}}{\hbar\omega_B} \quad |m,n+1\rangle\\
-\frac{(2m+1)\sqrt{n}}{\hbar\omega_B} \quad |m,n-1\rangle\\
-\frac{\sqrt{m}\sqrt{m-1}\sqrt{n+1}}{\hbar(2\omega_A-\omega_B)} \quad |m-2,n+1\rangle\\
-\frac{\sqrt{m}\sqrt{m-1}\sqrt{n}}{\hbar(2\omega_A+\omega_B)} \quad |m-2,n-1\rangle\Bigg),
\end{aligned}$$

where we make use of the fact that the energy spacings between subsequent levels are equidistant in zero-order, i.e., the harmonic energy spacings. Due to this regularity in the energy spectrum, we can rewrite this equation in terms of ladder operators in a basis-free representation:

$$|\psi_{m,n}\rangle = \left(\hat{I}+\lambda_{AAB}\hat{O}\right)|m,n\rangle, \qquad \text{(A5)}$$

where $\hat{I}$ is the identity operator, and $\hat{O}$ causes the perturbation:

$$\begin{aligned}
\hat{O} =& \frac{1}{2+w}2^{-3/2}\left(\hat{a}_A^{\dagger 2}\hat{a}_B^{\dagger}-\hat{a}_A^2\hat{a}_B\right) \qquad \text{(A6)}\\
&+\frac{1}{2-w}2^{-3/2}\left(\hat{a}_A^{\dagger 2}\hat{a}_B-\hat{a}_A^2\hat{a}_B^{\dagger}\right)\\
&+\frac{1}{w}2^{-3/2}(\hat{a}_A\hat{a}_A^{\dagger}+\hat{a}_A^{\dagger}\hat{a}_A)\left(\hat{a}_B^{\dagger}-\hat{a}_B\right).
\end{aligned}$$

The pre-factor $\hbar\omega_A$ is absorbed into the operator $\hat{O}$, which in turn only depends on the frequency ratio $\omega = \omega_B/\omega_A$.

An operator $\hat{A}$ can be expressed in the basis of perturbed wave functions $|\psi_{m,n}\rangle$. Since the operator $(\hat{I}+\lambda_{AAB}\hat{O})$ generates the perturbed wave function from the harmonic eigenstates, basis transform of the operator $\hat{A}$ is given by:

$$\langle\psi_{i,j}|\hat{A}|\psi_{k,l}\rangle = \langle i,j|\underbrace{\left(\hat{I}+\lambda_{AAB}\hat{O}\right)^{\dagger}\hat{A}\left(\hat{I}+\lambda_{AAB}\hat{O}\right)}_{\hat{A}^{\text{anh}}}|k,l\rangle. \qquad \text{(A7)}$$

Multiplying out the basis transformation while neglecting the λ_{AAB}^2 term, and making use of $\hat{O}^{\dagger}=-\hat{O}$ reduces the problem to the calculation of a commutator

$$\hat{A}^{\text{anh}} = \hat{A}^H + \lambda_{AAB}\left[\hat{A}^H,\hat{O}\right]. \qquad \text{(A8)}$$

This expression is solved easily for $\hat{A}=\hat{q}_A=1/\sqrt{2}(\hat{a}_A^{\dagger}+\hat{a}_A)$ and $\hat{A}=\hat{q}_B=1/\sqrt{2}(\hat{a}_B^{\dagger}+\hat{a}_B)$. Making use of the commutators $[\hat{a}_A,\hat{a}_A^{\dagger}]=1$ and $[\hat{a}_A,\hat{a}_B]=0$ finally gives:

$$\begin{aligned}
\left[\hat{q}_A,\hat{O}\right] =& W_1\left(\hat{a}_A\hat{a}_B+\hat{a}_A^{\dagger}\hat{a}_B^{\dagger}\right) \qquad \text{(A9)}\\
&+W_2\left(\hat{a}_A^{\dagger}\hat{a}_B+\hat{a}_A\hat{a}_B^{\dagger}\right)\\
\left[\hat{q}_B,\hat{O}\right] =& W_3\left(\hat{a}_A^{\dagger 2}+\hat{a}_A^2\right) \qquad \text{(A10)}\\
&+W_4\left(\hat{a}_A^{\dagger}\hat{a}_A+\hat{a}_A\hat{a}_A^{\dagger}\right)
\end{aligned}$$

with the frequency dependent scaling factors W_1 to W_4 given in Eq. 12.

[1] P. G. Debenedetti, J. Phys.- Condens Matter **15**, R1669 (2003).

[2] Y. Tanimura and S. Mukamel, J. Chem. Phys. **99**, 9496 (1993).

[3] S. Palese, J. T. Buontempo, L. Schilling, W. T. Lotshaw, Y. Tanimura, S. Mukamel, and R. J. D. Miller, J. Phys. Chem. **98**, 12466 (1994).
[4] K. Okumura and Y. Tanimura, J. Chem. Phys. **106**, 1687 (1997).
[5] K. Okumura and Y. Tanimura, Chem. Phys. Lett. **277**, 159 (1997).
[6] K. Okumura and Y. Tanimura, J. Chem. Phys. **107**, 2267 (1997).
[7] S. Saito and I. Ohmine, J. Chem. Phys. **108**, 240 (1998).
[8] A. Ma and R. M. Stratt, Phys. Rev. Lett. **85**, 1004 (2000).
[9] Y. Tanimura and T. Steffen, J. Phys. Soc. Japan **69**, 4095 (2000).
[10] T. l. C. Jansen, J. G. Snijders, and K. Duppen, J. Chem. Phys. **113**, 307 (2000).
[11] S. Saito and I. Ohmine, Phys. Rev. Lett. **88**, 207401 (2002).
[12] K. Okumura and Y. Tanimura, J. Phys. Chem. A **107**, 8092 (2003).
[13] S. Saito and I. Ohmine, J. Chem. Phys. **119**, 9073 (2003).
[14] S. Saito and I. Ohmine, J. Chem. Phys. **125**, 84506 (2006).
[15] Y. Tanimura, J. Phys. Soc. Japan **75**, 082001 (2006).
[16] Y. Nagata and Y. Tanimura, J. Chem. Phys. **124**, 24508 (2006).
[17] R. DeVane, C. Kasprzyk, B. Space, and T. Keyes, J. Phys. Chem B **110**, 3773 (2006).
[18] T. Hasegawa and Y. Tanimura, J. Chem. Phys. **125**, 074512 (2006).
[19] T. Yagasaki and S. Saito, Acc. Chem. Res. **42**, 1250 (2009).
[20] A. Tokmakoff, M. J. Lang, D. S. Larsen, G. R. Fleming, V. Chernyak, and S. Mukamel, Phys. Rev. Lett. **79**, 2702 (1997).
[21] D. A. Blank, L. J. Kaufman, and G. R. Fleming, J. Chem. Phys. **111**, 3105 (1999).
[22] D. A. Blank, L. J. Kaufman, and G. R. Fleming, J. Chem. Phys. **113**, 771 (2000).
[23] L. J. Kaufman, J. Heo, L. D. Ziegler, and G. R. Fleming, Phys. Rev. Lett. **88**, 207402 (2002).
[24] K. J. Kubarych, C. J. Milne, and R. J. D. Miller, Int. Rev. Phys. Chem. **22**, 497 (2003).
[25] O. Golonzka, N. Demirdöven, M. Khalil, and A. Tokmakoff, J. Chem. Phys. **113**, 9893 (2000).
[26] Y. L. Li, L. Huang, R. J. D. Miller, T. Hasegawa, and Y. Tanimura, J. Chem. Phys. **128**, 234507 (2008).
[27] H. Frostig, T. Bayer, N. Dudovic, Y. C. Eldar, and Y. Silberberg, Nat. Photon. **9**, 339 (2015).
[28] M. Cho, *Two-Dimensional Optical Spectroscopy* (CRC Press, Boca Raton, 2009).
[29] P. Hamm and M. T. Zanni, *Concepts and Methods of 2D Infrared Spectroscopy* (Cambridge University Press, Cambridge, 2011).
[30] W. Kuehn, K. Reimann, M. Woerner, and T. Elsaesser, J. Chem. Phys. **130**, 164503 (2009).
[31] W. Kuehn, K. Reimann, M. Woerner, T. Elsaesser, R. Hey, and U. Schade, Phys. Rev. Lett. **107**, 67401 (2011).
[32] W. Kuehn, K. Reimann, M. Woerner, T. Elsaesser, and R. Hey, J. Phys. Chem. B **115**, 5448 (2011).
[33] T. Elsaesser, K. Reimann, and M. Woerner, J. Chem. Phys. **142**, 212301 (2015).
[34] C. Somma, G. Folpini, K. Reimann, M. Woerner, and T. Elsaesser, J. Chem. Phys. **144**, 184202 (2015).
[35] J. Lu, Y. Zhang, H. Y. Hwang, B. K. Ofori-Okai, S. Fleischer, and K. A. Nelson, Proc. Natl. Acad. Sci. USA **113**, 11800 (2016).
[36] C. L. Johnson, B. E. Knighton, and J. A. Johnson, Phys. Rev. Lett. **122**, 73901 (2019).
[37] S. Houver, L. Huber, M. Savoini, E. Abreu, and S. L. Johnson, Opt. EXPRESS 10854 **27**, 10854 (2019).
[38] P. Hamm, M. Meuwly, S. L. Johnson, and P. Beaud, Struct. Dyn. **4**, 061601 (2017).
[39] D. J. Ulness, J. C. Kirkwood, and A. C. Albrecht, J. Chem. Phys. **108**, 3897 (1998).
[40] P. Hamm and J. Savolainen, J. Chem. Phys. **136**, 94516 (2012).
[41] P. Hamm, J. Savolainen, J. Ono, and Y. Tanimura, J. Chem. Phys. **136**, 236101 (2012).
[42] P. Hamm, J. Chem. Phys. **141**, 184201 (2014).
[43] J. Savolainen, S. Ahmed, and P. Hamm, Proc. Natl. Acad. Sci. **110**, 20402 (2013).
[44] A. Berger, G. Ciardi, D. Sidler, P. Hamm, and A. Shalit, Proc Natl. Acad. Sci. USA **116**, 2458 (2019).
[45] A. Shalit, S. Ahmed, J. Savolainen, and P. Hamm, Nat. Chem. **9**, 273 (2017).
[46] I. A. Finneran, R. Welsch, M. A. Allodi, T. F. Miller, and G. A. Blake, Proc. Natl. Acad. Sci. **113**, 6857 (2016).
[47] I. A. Finneran, R. Welsch, M. A. Allodi, T. F. Miller, and G. A. Blake, J. Phys. Chem. Lett. **8**, 4640 (2017).
[48] G. Ciardi, A. Berger, P. Hamm, and A. Shalit, J. Phys. Chem. Lett. **10**, 4463 (2019).
[49] C. H. Cho, J. Urquidi, S. Singh, and G. W. Robinson, J. Phys. Chem. B **103**, 1991 (1999).
[50] M. Cho, J. Chem. Phys. **111**, 4140 (1999).
[51] M. Cho, Phys. Rev. A - At. Mol. Opt. Phys. **61**, 023406 Theoretical (2000).
[52] H. Ito, T. Hasegawa, and Y. Tanimura, J. Chem. Phys. **141**, 124503 (2014).
[53] H. Ito, J. Y. Jo, and Y. Tanimura, Struct. Dyn. **2**, 054102 (2015).
[54] T. Ikeda, H. Ito, and Y. Tanimura, J. Chem. Phys. **142**, 212421 (2015).
[55] Z. Pan, T. Wu, T. Jin, Y. Liu, Y. Nagata, R. Zhang, and W. Zhuang, J. Chem. Phys. **142**, 212419 (2015).
[56] H. Ito and Y. Tanimura, J. Chem. Phys. **144**, 074201 (2016).
[57] H. Ito, T. Hasegawa, and Y. Tanimura, J .Phys. Chem. Lett. **7**, 4147 (2016).
[58] I. B. Magdău, G. J. Mead, G. A. Blake, and T. F. Miller, J. Phys. Chem. A **123**, 7278 (2019).
[59] D. Sidler and P. Hamm, J. Chem. Phys. **150**, 044202 (2019).
[60] P. Hamm, J. Chem. Phys. **151**, 054505 (2019).
[61] P. Hamm and A. Shalit, J. Chem. Phys. **146**, 130901 (2017).
[62] M. Khalil, N. Demirdöven, and A. Tokmakoff, Phys. Rev. Lett. **90**, 47401 (2003).
[63] D. Sidler, M. Meuwly, and P. Hamm, J. Chem. Phys. **148**, 244504 (2018).
[64] P. Tröster, K. Lorenzen, M. Schwörer, and P. Tavan, J. Phys. Chem. B **117**, 9486 (2013).
[65] J. S. Tse and M. L. Klein, Phys. Rev. Lett. **58**, 1672 (1987).
[66] H. Torii, Chem. Phys. Lett. **323**, 382 (2000).
[67] S. Ueno and Y. Tanimura, J. Chem. Theory Comput. **16**, 2099 (2020), arXiv:2002.10600.